ACS APPLIED MATERIALS & INTERFACES

www.acsami.org Research Article

Self-Powered Force Sensors for Multidimensional Tactile Sensing

Weiyi Zhang, Yuan Xi, Engui Wang, Xuecheng Qu, Yuan Yang, Yubo Fan,* Bojing Shi,* and Zhou Li*

Cite This: ACS Appl. Mater. Interfaces 2022, 14, 20122−20131 Read Online

ABSTRACT: A tactile sensor is the centerpiece in human−machine interfaces, enabling robotics or prosthetics to manipulate objects dexterously. Specifically, it is crucial to endow the sensor with the ability to detect and distinguish normal and shear forces in real time, so that slip detection and more complex control could be achieved during the interaction with objects. Here, a self-powered multidirectional force sensor (SMFS) based on triboelectric nanogenerators with a three-dimensional structure is proposed for sensing and analysis of normal and shear forces in real time. Four polydimethylsiloxane (PDMS) cylinders act as the force sensing structure of the SMFS. A flexible tip array made of carbon black/MXene/PDMS composites is used to generate triboelectric signals when the SMFS is driven by an external force. The SMFS can sense multidimensional force due to the adaptability of the PDMS cylinders and detect tiny force due to the sensitivity of the flexible tips. A small shear force as low as 50 mN could be recognized using the SMFS. The direction of the externally applied force could be recognized by analyzing the location and output voltage amplitude of the SMFS. Moreover, the tactile sensing applications, including reagent weighing and force direction perception, are also achieved by using the SMFS, which demonstrates the potential in promoting developments of self-powered wearable sensors, human−machine interactions, electronic skin, and soft robotic applications.

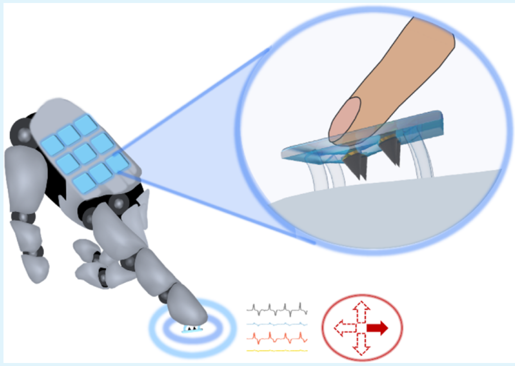

KEYWORDS: *shear force, tactile sensing, multidimensional force sensor, self-powered, TENG*

1. INTRODUCTION

Flexible force sensors are becoming increasingly important for tactile and biological mechanical force sensing in a large variety of applications, including health care, robotics, and human−machine interactions.[1−6] For instance, wearable and implantable force sensors detect the pulse rhythm and blood pressure to reflect the potential cardiovascular disease.[7−9] Also, for robotics, force sensors will enable the function of object perception, which is also a promising device to realize human−machine interactions.[10−12] Up to now, there have been many reports focusing on designing the microstructure and improving the sensing materials to increase the sensitivity of force sensors.[13−15] Most of the sensors respond to unidirectional force; however, the ability to detect and distinguish normal and shear forces in real time is crucial to provide important information in practice. These parameters cannot be directly obtained with the traditional force sensors, while future force sensors are required to perform integrated sensing capabilities for manipulation tasks like realizing automation of experimental operations with robotic hands.[16−18] Hence, to achieve higher manipulative and intelligent levels of force sensing applications, an integrated force sensor that could sense the value and directions of force simultaneously is an inspiring and challenging research topic.[19−21]

Various types of force sensors have been explored, based on piezoresistive, capacitive, piezoelectric, and triboelectric mechanisms.[22−24] These sensors could transform the force change into resistance, capacitance, and voltage or current responses, respectively. Among them, triboelectric nanogenerators (TENGs) could be a promising candidate for pressure sensors because of their broad material selections, simple structure, low cost, and high power density.[25−27] The working principle of triboelectric active sensors is also based on the triboelectric effect and electrostatic induction. In addition, to meet the requirement of simultaneously detecting the force amplitudes and directions, researchers conducted their studies on microstructured capacitive sensors and dual-mode sensors combined with piezoresistive and capacitive modes or piezoresistive and piezoelectric modes.[28−30] Here, we focus on realizing the function of normal and shear force detection using TENGs in this research.

Nevertheless, choosing suitable materials for high-performance triboelectric force sensors remains a great challenge. Polydimethylsiloxane (PDMS) has been widely used in TENGs as a triboelectrification layer or a matrix for

Received: March 1, 2022
Accepted: April 12, 2022
Published: April 22, 2022

https://doi.org/10.1021/acsami.2c03812
ACS Appl. Mater. Interfaces 2022, 14, 20122−20131

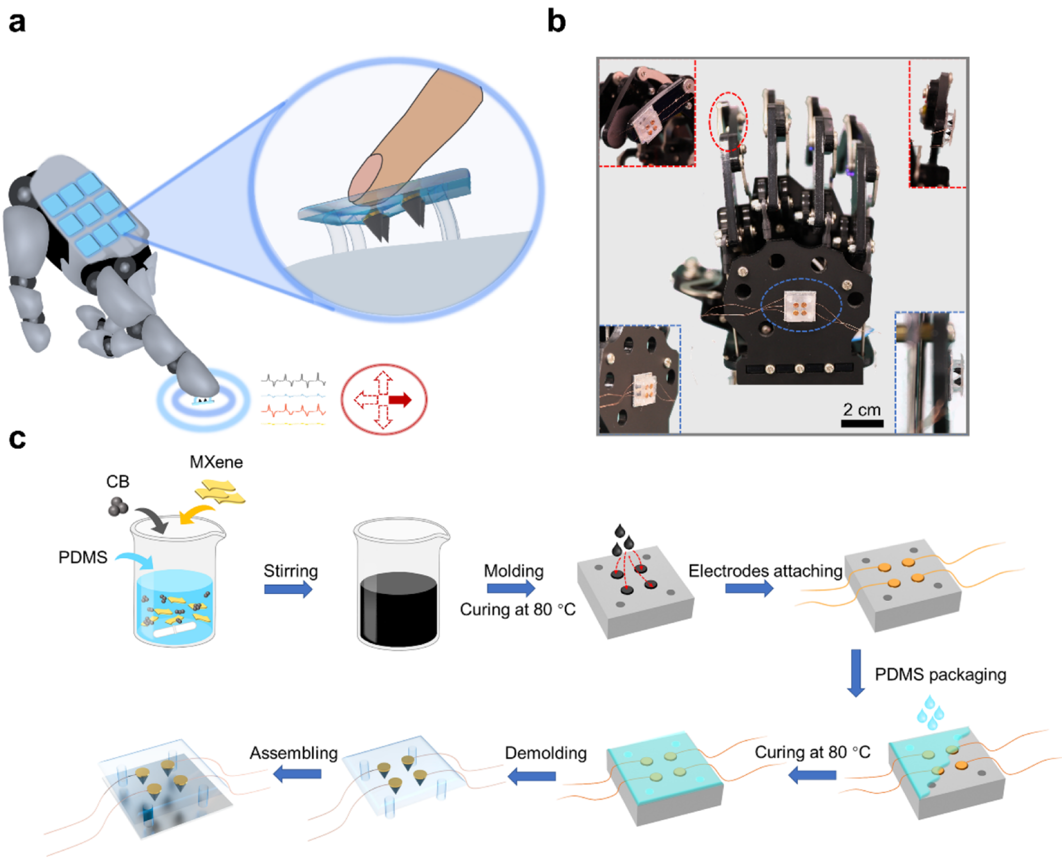

Figure 1. Overview of SMFSs. (a) Schematic illustration showing SMFS working as a human−machine interface. (b) Digital photographs of the SMFS attached to the index finger (the red dotted line) and the back (the blue dotted line) of a robotic hand. (c) Schematic diagram of fabrication process of the SMFS based on CB/Mxene/PDMS composites.

composites with excellent flexibility, electronegativity, and biocompatibility. To further enhance the sensitivity of PDMS-based triboelectric pressure sensors, numerous approaches have been performed. One of these effective methods is doping a suitable amount of conductive fillers in PDMS, such as carbon black (CB), graphene sheets, and carbon nanotubes, so that the surface charge density will be increased by the increased capacitance of the TENG and reduced internal resistance of PDMS.[31−33] As a result, the sensitivity of triboelectric pressure sensors can be improved by increasing the peak output voltage. Among these fillers, CB has been considered as a good filler, owing to its high conductivity, easy availability, low cost, and low specific weight. Due to the charge storage ability of CB, CB-doped composites have been proved to be effective in enhancing the output performance of the TENG; however, the enhancement is still limited. In addition, owing to its highly conductive and electronegative properties and excellent mechanical stability, MXene (e.g., titanium carbide and $Ti_3C_2T_x$, where T_x is O, OH, or F) has been considered as a new effective conductive filler for fabricating high-power output TENGs.[34−36] Therefore, a strategy for utilizing the additive effect of MXene and further improving the output of the triboelectric pressure sensors is required.

Herein, we report a self-powered multidirectional force sensor that can detect and distinguish normal, tilt, and shear forces, which is based on the contact-separating mode TENG. The sensor is composed of a flexible PDMS cylinder supporting structure and sensing structure. Moreover, the mechanical and electrical properties of three different sensing structures, including the cylinder, cuboid, and cone, were measured and compared. The cone was proved to be the proper sensing structure and was further improved by doping CB and MXene into PDMS, resulting in an increased output voltage, good linearity, and fast response under an applied force. Besides, the sensing signals from four cones could be recorded and analyzed according to the location and voltage amplitude of each cone, and thus, the direction of applied force could be realized. Furthermore, the reagent weighing in a test tube and force direction perception for a smart indication system were achieved as tactile sensing applications, illustrating the excellent potential for development in self-powered wearable sensors and human−machine interfaces.

2. RESULTS AND DISCUSSION

2.1. Fabrication of the SMFS and its Characterization. Figure 1a illustrates the schematic diagram of the SMFS, which is working as a human−machine interface. The detected signals from the sensor could be recorded and analyzed for providing feedback by artificial intelligence. As shown in Figure 1b, the SMFS can be attached to different parts of a robotic hand to achieve human−machine interface applications. Besides, the fabrication process of the SMFS is shown in Figure 1c. First, a diluted solution of PDMS and hexane was mixed thoroughly with CB and MXene. The solution was stirred until the CB and MXene were uniformly mixed with PDMS and hexane was evaporated. Next, a cross-linker was added to the above solution at a mass ratio of 10:1 with PDMS

https://doi.org/10.1021/acsami.2c03812
ACS Appl. Mater. Interfaces 2022, 14, 20122−20131

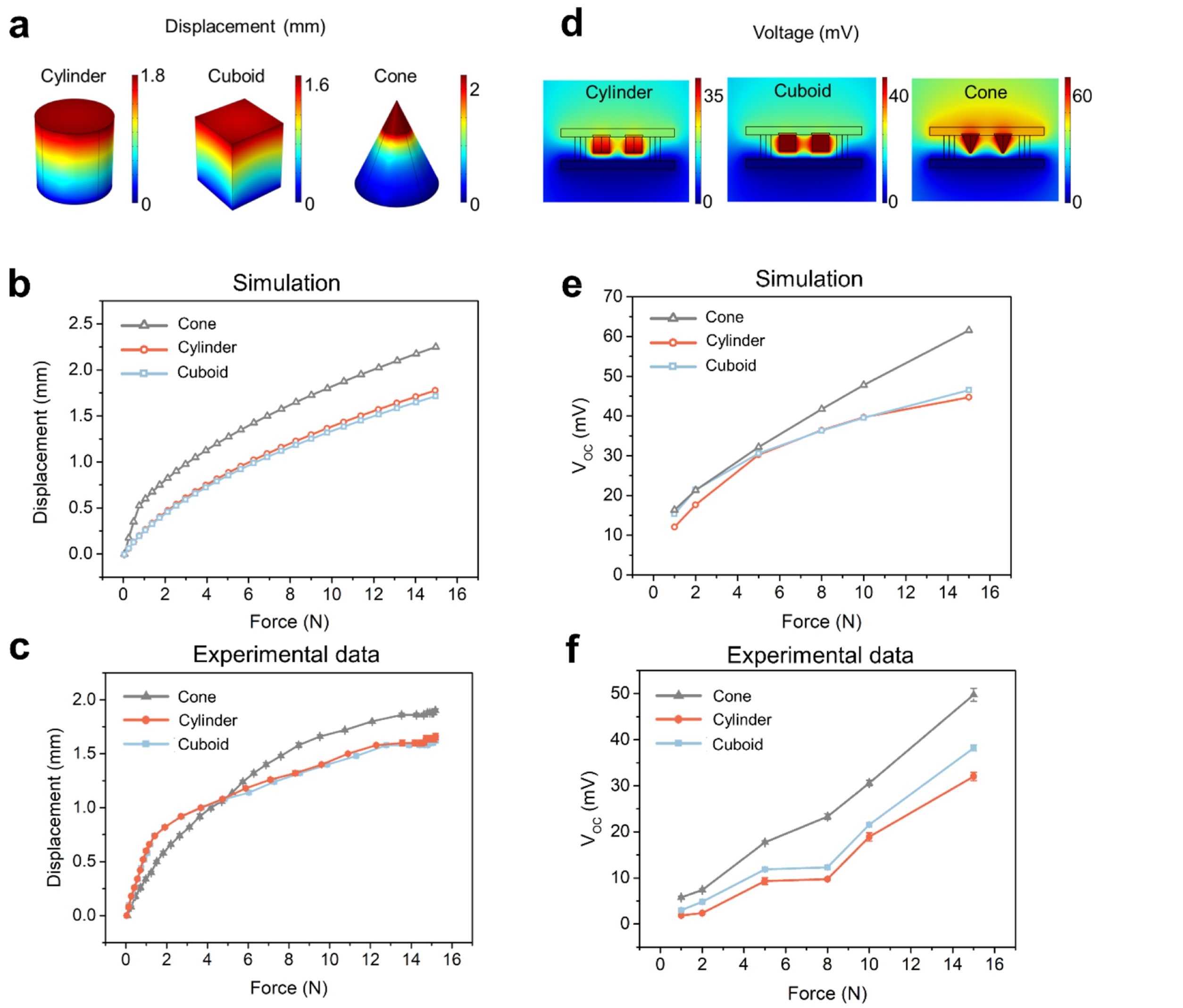

Figure 2. Mechanical and electrical properties of SMFSs. (a,b) Simulation results showing force−displacement relationship of different sensing structures under normal force. (c) Corresponding experimental data for force−displacement relationship. (d,e) Simulation results showing mechano−electrical relationship of different sensing structures. (f) Corresponding experimental data for mechano−electrical relationship.

base. Afterward, the composite consisting of CB, MXene, and PDMS was drop cast and degassed in a PTFE mold with cone structures and cured at 80 °C. Four round copper electrodes with copper wires were then attached to the upper surface of the cones. The pure PDMS prepolymer, composed of a polymer base and curing agent with a mass ratio of 10:1, was used to encapsulate the cones and electrodes and to fill into the empty cylinders in the mold. These cylinders were regarded as the supporting structure of the sensor after curing. As a result, an integrated structure with sensing and supporting structures was achieved after the curing and demolding process. By using a similar fabrication method, the CB/PDMS composite with a cone sensing structure and pure PDMS with cylinder, cuboid, and cone structures were also fabricated for comparison. Finally, the integrated structure was assembled with a bottom electrode by pasting the supporting cylinders on an aluminum (Al) foil-coated positron emission tomography (PET) substrate.

We fabricated CB/PDMS and CB/MXene/PDMS composites with various CB (1, 2, 5, 10, and 15 wt %) and MXene (1, 2, 3, and 4 wt %) mass ratios in PDMS. For simplicity, the composite-based SMFSs were named "C_xM_y" according to the content of CB and MXene, where x and y represent the content of CB and MXene, respectively. For example, C_1 means 1 wt % CB-doped PDMS and C_2M_1 means 2 wt % and 1 wt % MXene-doped PDMS. The surface morphology of these samples is shown in Figure S1. Aside from C_{10} and C_{15}, there is a slight aggregation of C_5. In addition, there is no significant difference in surface morphology of other samples due to the low doping ratio, indicating a homogeneous composite of CB and PDMS. Even though the mass ratios of C_{10} and C_{15} are a little higher, CB was also dispersed uniformly in PDMS, as can be seen in Figure S1. To confirm the well mixing of the MXene in the composite, the cross-section view and element mapping of the selected zone of C_2M_3 are shown in Figure S2. The strong titanium (Ti) signal belonging to MXene indicates that MXene has been well embedded in the PDMS matrix. The fluorine (F) signal verifies the existence of active −F groups in MXene.

2.2. Design and Optimization of the SMFS. To improve sensor performance by generating more charges through contact electrification, the active layer microengineering of triboelectric pressure sensors has attracted much interest and is becoming increasingly important in sensor structure designing.

https://doi.org/10.1021/acsami.2c03812
ACS Appl. Mater. Interfaces 2022, 14, 20122−20131

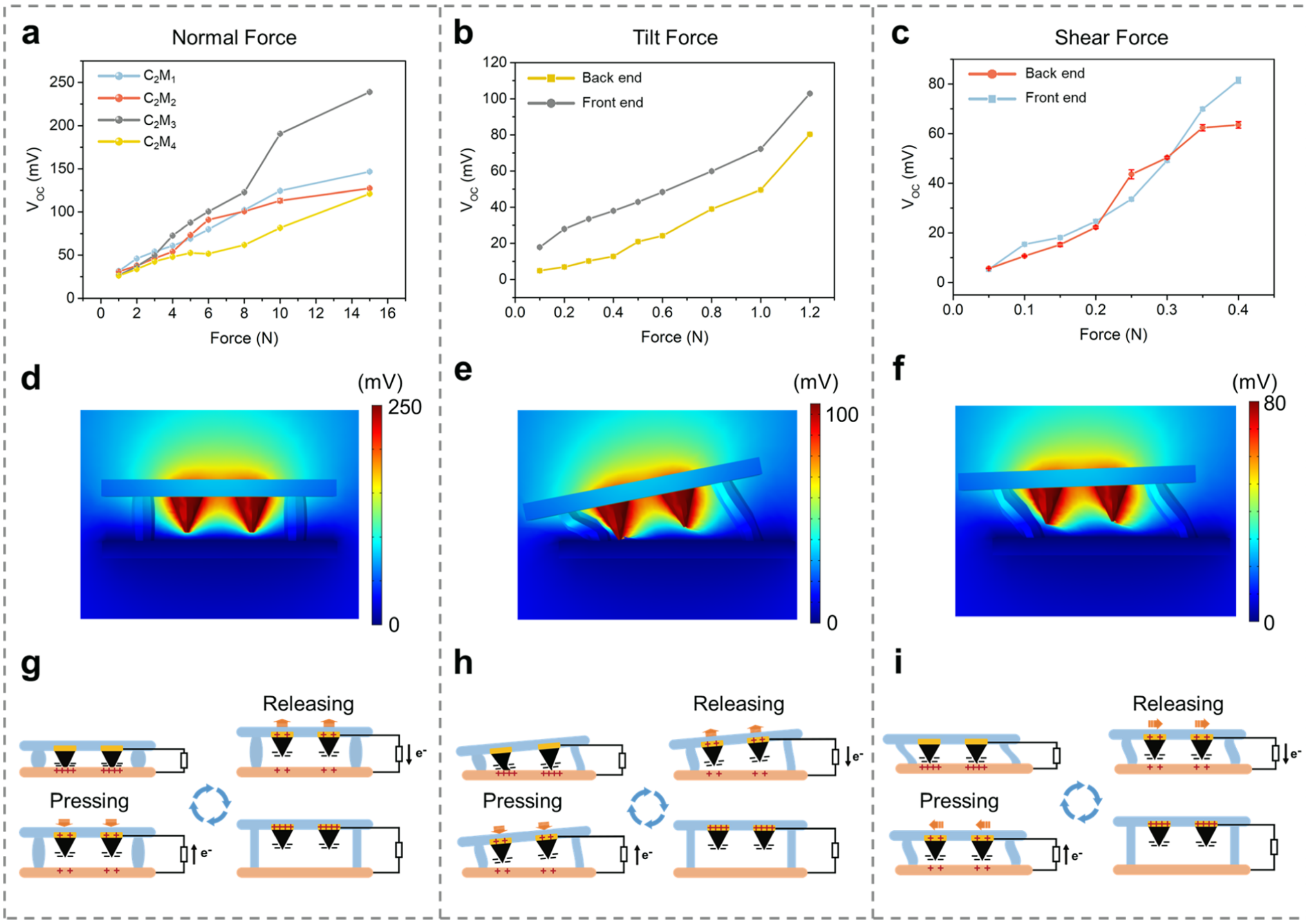

Figure 3. V_{OC} responses of SMFSs with different CB/MXene contents under (a) normal force ranging from 1 to 15 N. V_{OC} responses of C_2M_3 under (b) tilt force ranging from 0.1 to 1.2 N and (c) shear force ranging from 0.05 to 0.4 N. (d−f) Simulation results of electrical potential distributions of C_2M_3 under normal, tilt, and shear forces. (g−i) Schematics of the sensing principle for C_2M_3 under normal, tilt, and shear forces.

Because various microstructures will lead to different non-uniform stress distributions during the pressure sensing, a variety of microstructures have been investigated according to the needs. In this work, we compared the mechanical properties and triboelectric voltage output of cylinder, cuboid, and cone sensing structures by finite element analysis and experimental results. The comparison of mechanical properties was studied. In the simulation, the height of the cylinder, cuboid, and cone was kept the same; the size of the base radius of the cone and cylinder and the bottom side length of the cuboid were also kept consistent, while the contact surface area was varied. Figure 2a shows the same compressing state of three sensing structures made of pure PDMS. From the simulation results, including the displacement distribution in Figure 2a and curves plotted in Figure 2b, the sensing part with the cone structure has the largest deformation under the same normal force, which means that the smaller the contact surface area, the larger the degree of deformation under normal pressure could be achieved. The cone has better performance than other shapes like the cylinder and cuboid because of its non-uniform stress distribution, which concentrates at its pointed tip. The tips of the cones will compress more for a given applied pressure, resulting in higher mechanical deformations and consequently sensitivities.[17,37] To verify this simulation result, corresponding samples with different sensing structures are fabricated. The experimental result in Figure 2c shows that the deformation results of the three samples have a similar variation trend under normal force. Even though their displacements are almost the same under low pressure, the cone structure has the largest deformation with the increase in normal force eventually.

When it comes to the comparison of triboelectric voltage output, the simulation of the potential distribution in successive press-release cycles is also studied for cylinder, cuboid, and cone sensing structures. The process of the dynamic press-release cycle and potential distribution for three sensing structures are shown in Video S1. When the sensing structures approach, press, or separate from the Al electrode, the electric potential difference accordingly changes. Three representative results of three sensing structures in the same pressing state are presented in Figure 2d. Compared with the other two samples, the cone sensing structure possesses the largest potential difference during the press-release cycles, and the voltage outputs are thereby the highest over the applied normal force range, as shown in Figure 2e. Corresponding experiments were also conducted to validate the simulation results. The experimental setup for the normal force test is shown in Figure S3. The experimental result in Figure 2f shows that the open-circuit voltage (V_{OC}) of the cone sample is the highest, the cuboid comes second, and the cylinder has the lowest V_{OC} output, which is in good accordance with the simulation result. Some representative response curves of the

https://doi.org/10.1021/acsami.2c03812
ACS Appl. Mater. Interfaces 2022, 14, 20122−20131

cylinder, cuboid, and cone sensing structure are shown in Figure S4. The specific mechanism and potential variation process of the triboelectric pressure sensor will be discussed in detail in the working mechanism section. After studying the effect of the sensing structures on mechanical characteristics and electrical outputs of the triboelectric pressure sensors, the cone has been proved as the optimal sensing structure for pressure sensing in this work, and thus, the sensitivity improvement by sensing material optimization can be better explored based on this result.

To improve the triboelectric pressure sensing performance, SMFSs based on the different mass ratios of CB/MXene/PDMS composites were fabricated to investigate the optimal sensing performance under normal force. CB has been proved to be effective to improve the output performance of TENGs as a doping agent. The SMFSs made of CB-doped PDMS without MXene were first tested under normal force. Here, CB content of 1, 2, 5, 10, and 15 wt % was selected for comparison. Due to the uniform arrangement of the four cone sensing structures, the normal force was uniformly applied to each of them; every cone had similar V_{OC} output, so the generated V_{OC} of one cone is shown for comparison. Figure S5 demonstrates the relationship between generated V_{OC} and applied normal force of the CB/PDMS-based sensor. The V_{OC} gradually increases as the applied normal force changes from 1 to 15 N at a compression speed of 100 mm/min. Compared with pure PDMS, the introduction of CB into PDMS improves the outputs of the SMFS at a low CB mass ratio. When the CB content is 1 wt %, obvious improvement is observed. This is because CB plays a role as a charge trapping site and it increases the dielectric constant of the contact layer, and thus, it can increase the total amount of the involving negative electrical charges in the contact layer of the TENG. The V_{OC} output reaches its maximum value when the content is 2 wt % over a range of applied normal force. With the further increase in CB content, there will be a negative effect on sensing performance. When the CB content is greater than 5 wt %, the V_{OC} outputs under the applied force gradually decrease with the addition of CB. This result could be attributed to the excessive amount of the CB in PDMS, which cannot effectively store the charges due to the formation of CB agglomeration, resulting in leakage current and lower V_{OC} outputs of C_{10} and C_{15} than those of pure PDMS (C_0). Therefore, in terms of the sensitivity comparison shown in Figure S5, the optimal CB content is observed to be 2 wt %. However, the increase in the sensitivity and the sensing resolution in a low pressure range is still limited by only doping CB in PDMS.

MXene exhibits a highly electronegative surface, which is attributed to the abundant −F groups and terminating functional groups containing oxygen. Thus, MXene becomes a promising alternative of electronegative material for TENGs to provide enhanced performance. To achieve the improvement of electrical performance from an additive effect with the incorporation of MXene, the different mass ratios between MXene and optimal CB content in PDMS were studied to acquire the optimal performance for SMFS sensing. The tests were also conducted under different cyclic normal compressive forces at 100 mm/min. Here, C_2M_1, C_2M_2, C_2M_3, and C_2M_4 were tested.

2.3. Mechanism of Multidirectional Force Sensing. As shown in Figure 3a, when the normal force is less than 3 N, these four sensors have almost the same responses. Starting from 4 N, the C_2M_3 possesses higher V_{OC} responses than those of other sensors under up to 15 N normal force. The V_{OC} improvement could be ascribed to the following reasons. First, MXene has similar electronegativity with PTFE due to the existence of −F groups, and the amount of charge transfer and V_{OC} are dependent on the difference in the electronegativities between the bottom Al electrode and sensing materials. Second, the presence of MXene, together with CB, could further decrease the internal resistance and enhance the capacitance of the CB/MXene/PDMS composite, thus leading to improved voltage output. The C_2M_4 has the lowest voltage output throughout the range of applied normal force, meaning that there is a negative impact on the performance when the mass ratio of MXene exceeds 3 wt %. It is similar to the impact caused by CB; at higher doping concentrations, MXene is likely to form aggregations, resulting in a conductive network composed of MXene and CB, thereby destroying the dielectric properties of PDMS. As a result, leaking electricity may lead to a decrease in voltage output under applied normal force. Based on the above results and analysis, C_2M_3 was chosen as an optimal device for further mechano−electrical tests.

An important function of the proposed SMFS is the ability to realize the direction of applied force. To investigate the V_{OC} responses of SMFSs to the applied tilt force and shear force besides normal force, corresponding pressure-sensing measurement apparatuses were set up (Figure S3). Like the apparatus for measuring normal force, the tilt force test setup was also constructed using a computer-controlled force gauge but with one oblique plane of 45° fixed at the bottom of the force gauge and the other one fixed on the platform. For the shear force, similarly, two perpendicular planes were attached to the bottom of the force gauge and the platform. The SMFS was fixed on the plane which was on the platform; by varying the top and bottom planes with different angles, normal force, tilt force, and shear force could be applied to the sensor through the vertical movement of the force gauge. During the test, from a vertical aspect, the cones at the lower location were marked as front ends, the upper ones were marked as back ends, as the samples shown in Figure S3. Note that the supporting structures of SMFSs are soft and flexible and will easily bend under tilt and shear forces, so the sensing structures could contact the Al electrode and be pressed much more easily. Compared to vertical compression of the SMFS under normal force, a small tilt or shear force could produce a relatively large displacement of the SMFS, namely, to achieve the same magnitude of displacement, the required tilt or shear force is much less than the normal force, as shown in Figure S6. As a result, the SMFS is capable of detecting slight tilt or shear force in different application scenarios, which will be shown in the applications section. As shown in Figure 3b, the SMFS generates V_{OC} responses to 45° tilt forces from 0.1 to 1.2 N. Although the variation trends of the V_{OC} under 45° tilt force are almost the same, the cone located at the front end generated a little higher V_{OC} output than the cone at the back end. This could be attributed to the location difference of the cones. Under the tilt force, the front-end cone will contact the bottom Al electrode first and deform more than the back-end one, so there will be a response difference observed in the experimental results, which implies that the SMFS has the potential of distinguishing the direction of applied force according to the V_{OC} response signal. When it comes to the shear force, the front- and back-end cones possess similar V_{OC} responses under the applied force ranging from 0.05 to 0.4 N (Figure 3c). In this situation, because the force was applied in a

https://doi.org/10.1021/acsami.2c03812
ACS Appl. Mater. Interfaces 2022, 14, 20122−20131

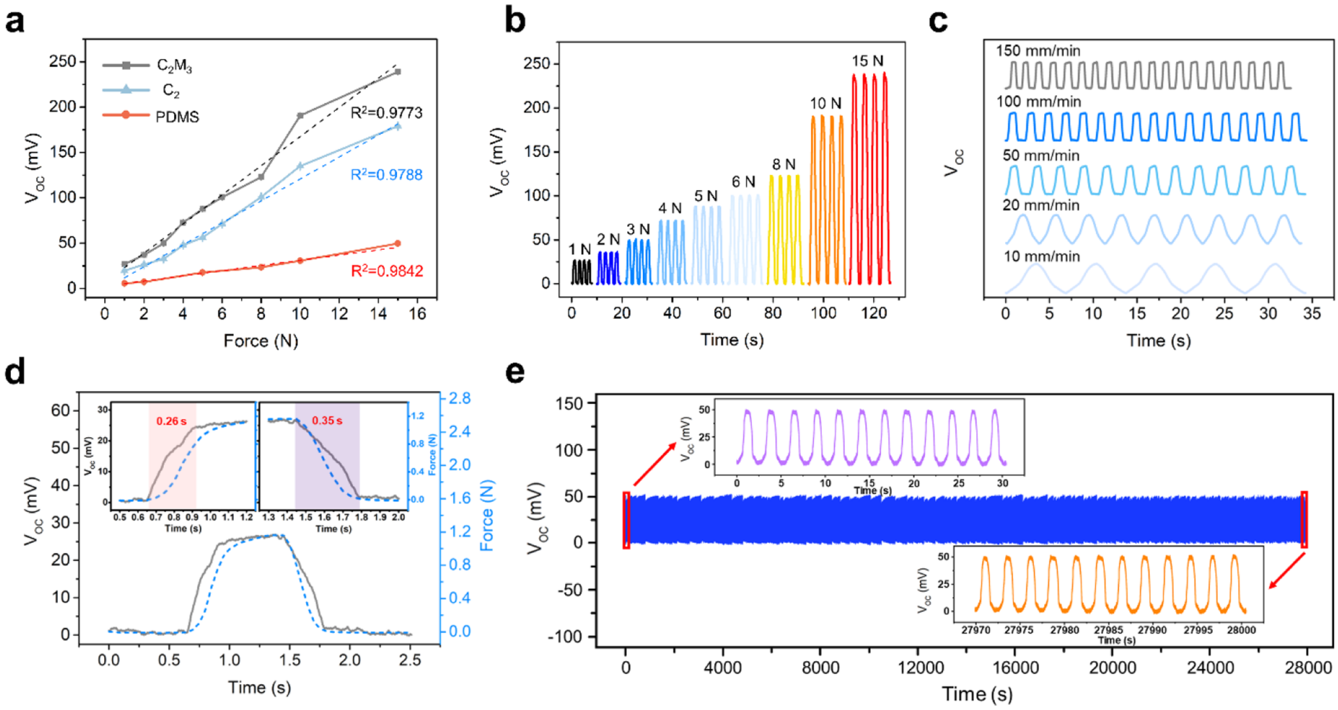

Figure 4. Properties of SMFSs with C_2M_3. (a) Mechano−electrical curves of C_2M_3 under serial normal forces ranging from 1 to 15 N. (b) V_{OC} responses of SMFSs at different operating speeds under 2 N. (c) V_{OC} responses and applied force curves under periodic loading and unloading cycles. (d) Response and recovery time of C_2M_3 under 1 N. (e) Cyclic stability of C_2M_3 under more than 10,000 cycles with an applied normal force of 3 N.

tangential direction, there was no significant difference between the cones at the front and back end, leading to similar V_{OC} outputs under the applied shear forces. However, the V_{OC} responses increase with the increase in applied force, indicating good sensing ability and resolution of slight shear force detected by SMFSs. Some representative response curves of SMFSs under tilt and shear forces are also shown in Figure S7. In addition, the relationship between the V_{OC} responses of the SMFSs and calculated applied pressure in Figure 3a−c is also summarized in Figure S8. More importantly, the minimum limit of shear force detection with C_2M_3 is 255 Pa (50 mN), as shown in Figure S8c, indicating good sensing ability of tiny shear force.

To elucidate the underlying sensing mechanism of the multidirectional pressure sensing, the corresponding simulation using COMSOL was first carried out. The deformations and potential distributions of the SMFS under normal, tilt, and shear forces are shown in Figure 3d−f, respectively. First, under the normal force, each cone exhibits the same potential and the SMFS could sustain a relatively large normal force. In addition, because of the three-dimensional geometry of the four-cone array and the anisotropic deformation of the sensing structure with applied tilt force, the cones located on the same side with the direction of applied force (front end) will be exposed to greater pressure, leading to a higher output voltage, compared to those located on the side opposite the applied force direction (back end). This result also applies to the situation of shear force, but the difference in output voltages between front-end and back-end cones is not obvious due to the similar pressure applied to them. According to the simulation results, the maximum potentials under normal, tilt, and shear forces are 250, 100, and 80 mV, respectively, which are in good accordance with the experimental results in Figure 3a−c.

Furthermore, the schematic diagram of the working principle of the SMFS is demonstrated when the normal, tilt, and shear forces are applied, as shown in Figure 3g−i. In general, when the top cones contact with the bottom Al electrode, owing to the triboelectrification effect and the strong electronegativity of CB/MXene/PDMS composites, negative charges are induced, while the triboelectric charges with opposite polarities are generated from the Al electrode. As the cones start to separate from the Al surface with the released forces, electrons transfer in the external load to eliminate the potential difference generated by charge induction. When the applied forces are released, a new balance between positive and negative charges is established. As the cones approach the Al electrode again, the electrons will flow back to form a reverse output signal. This working principle is suitable for these three situations, including normal, tilt, and shear forces. However, the cones contact the Al electrode in different ways. Specifically, the normal force causes deformation of the SMFS in the vertical direction, which will lead to an increased contact area of the pressed cones in the same direction. Tilt force enables the cones to contact with the Al electrode in an oblique way, which means that there is not only the increased contact area from the pressed cones but also the additional contact area brought by the contact between the side of the cones and the Al electrode. For the shear forces, slight deformation occurs at the tip of the cones, but the additional contact area mentioned above is still applicable to this situation. Hence, the shear forces could be detected by monitoring the corresponding output voltages under press-release cycles.

https://doi.org/10.1021/acsami.2c03812
ACS Appl. Mater. Interfaces 2022, 14, 20122−20131

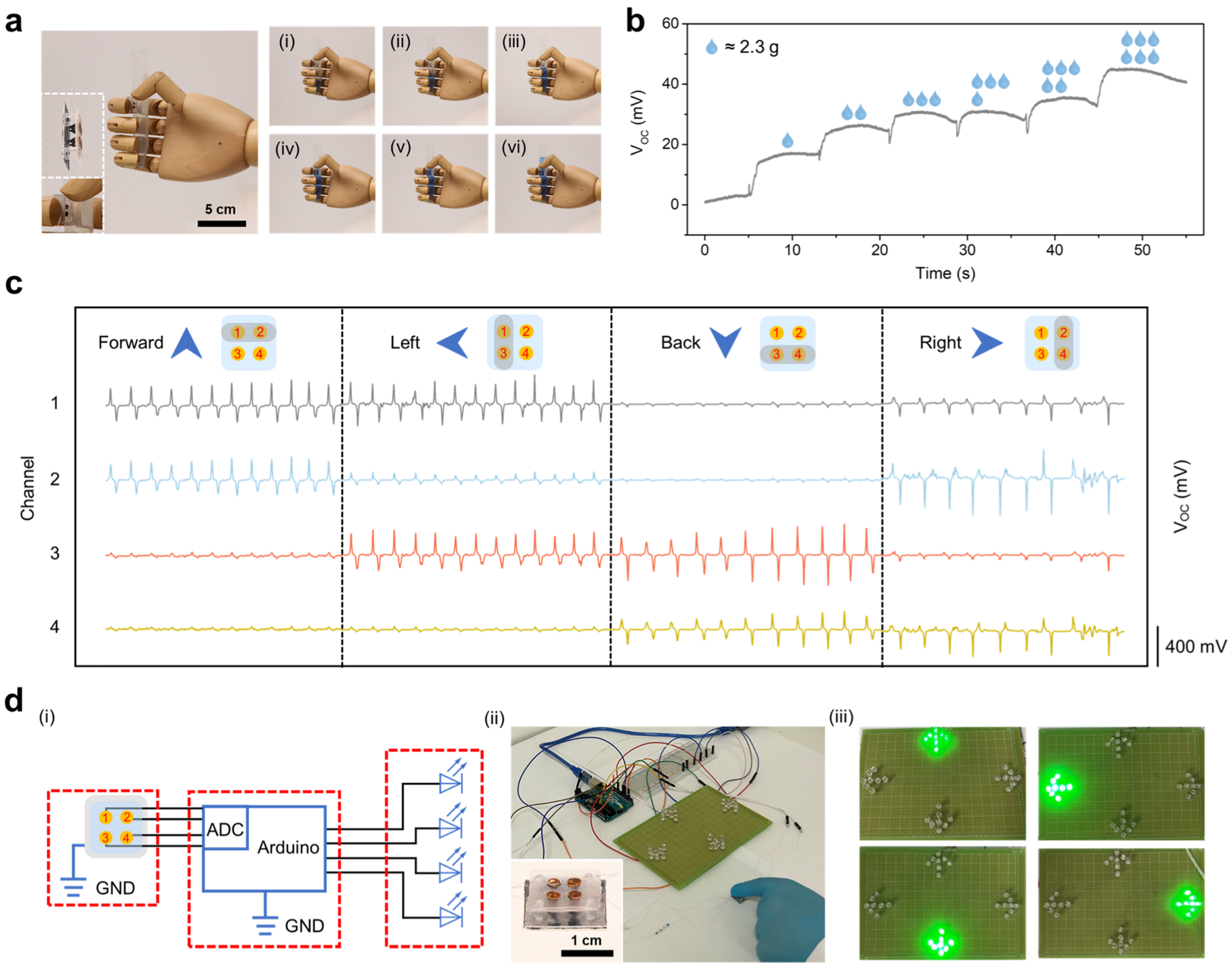

Figure 5. Demonstrations of SMFSs showing the ability to detect tilt and shear forces. (a) Digital photographs of the artificial hand equipped with the SMFS holding a test tube. (i–vi) Test tube was filled step by step. (b) V_{OC} responses and variations on addition of water six times. (c) Ability of distinguishing direction of tilt forces according to location and amplitude of the signal channel. (d) Smart indication system indicating direction of applied force by visually lighting arrows made of LEDs.

2.4. Normal Force Sensing Performance of the SMFS.

In addition to differentiation of tilt force and shear force, systematic mechano−electrical experiments under normal force for SMFSs were also conducted. First, when comparing the V_{OC} output of C_2M_3, C_2, and pure PDMS throughout normal force application, there is a considerable improvement that could be observed by adding CB and MXene at an optimal concentration. The V_{OC} responses of the cone sensing structure made of C_2M_3, C_2, and PDMS under applied normal force and corresponding applied pressure are shown in Figures 4a and S9, respectively. The response linearity of the C_2M_3, C_2, and pure PDMS-based sensor is calculated to be 0.9773, 0.9788, and 0.9842, respectively (Figure 4a). Moreover, by calculating the maximum ΔV_{OC} under applied pressure in Figure S9, the sensitivity of the C_2M_3 (2.97 mV kPa^{-1}) is 4.8 times higher than that of the PDMS-based sensor (0.62 mV kPa^{-1}) in the pressure range of 5.1−76.5 kPa. Figure 4b shows the V_{OC} response curves upon serially applied normal force. As the force increases, the V_{OC} gradually increases, indicating that more charges are transferred between the C_2M_3 cone and the Al electrode. The peak values of V_{OC} outputs are monotonically increasing and in good accordance with the result in Figures 3a and 3a. Therefore, the SMFS can precisely recognize the strength of the applied pressure by differentiating the amplitude of the V_{OC}. To further investigate the sensing ability of the SMFS, the dependence of the V_{OC} output of the C_2M_3 on the operating speed was tested. The applied normal force was set to 2 N. As shown in Figure 4c, the peak value of the V_{OC} showed negligible change with the operating speeds ranging from 10 to 150 mm/min, attributed to the saturation of tribocharges on the C_2M_3 surface,[38] exhibiting excellent uniformity and stability.

Additionally, another two key performance parameters of the pressure sensor are the response time and recovery time. The definition of response time is the time a sensor would take to reach 90% of its final signal amplitude upon an applied pressure; once the applied pressure is removed, the time for the sensor to recover to its original value is defined as recovery time. A complete cycle of V_{OC} response under loading and unloading of ∼1 N normal force and the corresponding applied force curve are plotted in Figure 4d. It is estimated that the V_{OC} response time and the recovery time are 0.26 and 0.35 s, respectively. There is no obvious delay between the loading/unloading time of the applied force and V_{OC} response/recovery

https://doi.org/10.1021/acsami.2c03812
ACS Appl. Mater. Interfaces 2022, 14, 20122−20131

time, as shown in Figure 4d. It should be noted that the response and the recovery time did not reach a millisecond level due to the moving speed of the force gauge. For the loading and unloading cycle of ~1 N force, which is also shown in Figure S10, the force gauge took 1.16 s to complete one cycle of ~1 N, so the response time and the recovery time of the SMFS are sufficient to meet the requirements of actual applications. Moreover, the real-time cyclic 8 N normal force and corresponding V_{OC} responses are shown in the same plot, and both plots match well (Figure S11). Therefore, the V_{OC} response of the SMFS could reveal detailed information about the press-release process of the applied force. To investigate the durability and stability of the C_2M_3-based SMFS, more than 10,000 loading and unloading cycles for 28,000 s were performed under 3 N at 150 mm/min, as shown in Figure 4e. During the starting and ending cycles in the magnified insets, the SMFS has very stable responses, and no obvious deterioration was observed during the test, confirming the good potential for applications.

2.5. Applications of Multidirectional Pressure Sensing. Considering the good sensitivity and the capability of tilt and shear force sensing, corresponding demonstrations were conducted to show the sensing ability of the SMFS in practice. First, an experiment of an artificial hand application scenario was performed to demonstrate the use of the SMFS in reagent weighing in real time. The SMFS was mounted on the index finger of an artificial hand, which was set to hold a test tube vertically. As shown in Figure 5a, at the original state, the top surface of the SMFS was in contact with the sidewall of the test tube. Subsequently, water was added into the test tube six times using a pipette to increase the weight. At each time, the additional volume of the water was around 2.3 g. Because the test tube was vertically held by the artificial hand, the added weight of the water was considered to be transferred to the shear force between the SMFS and the test tube, and the shear force was the only variable in this process. As shown in Figure 5b, the V_{OC} of the sensor increased with the water addition each time, and from the data recorded using an electrometer, the V_{OC} almost remained at each state after the water addition. The corresponding state of the test tube at each stage can be seen in (i−vi) steps of Figure 5a. As a result, the SMFS has proved to be capable of reagent weighing and has the potential to be substituted for humans in experimental operations.

Then, the ability to distinguish the direction of tilt force is shown in Figure 5c. Four top electrodes of the SMFS were connected with four data channels of an oscilloscope in sequence, and the sensing data were directly recorded using an oscilloscope and revealed on a screen in real time (Figure S12). The tilt force applied to the sensor was achieved by directionally pressing the sensor with a finger. The press action in each direction was repeated several times. As shown in Figure 5c and Video S2, the force direction can be clearly distinguished by comparing the amplitude of the four-channel V_{OC}. For example, when a forward force is exerted on the sensor, more force will concentrate on cone 1 and 2, leading to more deformation and higher voltage outputs, compared with those of cone 3 and 4. Therefore, by analyzing the amplitude of the V_{OC} of each cone, the force direction can be differentiated. Figure S13 illustrates the V_{OC} responses of a pixelated SMFS under the external force in a different direction.

3. CONCLUSIONS

In summary, based on the three-dimensional configuration with a supporting and sensing structure, we have developed a self-powered triboelectric SMFS that can detect and differentiate the normal and shear forces. Different sensing structures were fabricated and compared to optimize the sensor configuration. The corresponding sensing mechanism was also discussed. With the improvement of the sensing material, the CB/MXene/PDMS composite enhanced the sensing performance of the SMFS, resulting in increased voltage output, good linearity (R^2 = 0.9773), and fast response under an applied force. The sensitivity of the optimal device for normal force detection (2.97 mV kPa^{-1}) is 4.8 times higher than that of the PDMS cone sensing structure (0.62 mV kPa^{-1}) in the pressure range of 5.1−76.5 kPa. Also, a small shear force as low as 255 Pa could be recognized using the SMFS. By differentiating the location and output voltage amplitude, the direction of applied force could be realized and further utilized. In particular, based on the advantages of the SMFS, it can be used for measuring the reagent weight in real time and achieving a smart indication system. Therefore, the proposed SMFS has great potential as a self-powered sensor for human−machine interfaces, next-generation wearable electronics, and robotics in the future.

4. EXPERIMENTAL SECTION

4.1. Fabrication of the CB/PDMS and CB/MXene/PDMS. CB was purchased from Carbot Corporation with an average particle size of 50 nm. The CB/PDMS composite was prepared by mixing CB and PDMS (Sylgard 184, Dow Corning). To uniformly disperse the CB in PDMS matrix, the PDMS base material was first diluted in hexane; next, the CB was added to the diluted PDMS solution with different mass fractions (1, 2, 5, 10, and 15 wt %) and stirred thoroughly for 3 h to achieve a uniform mixture and evaporate hexane. The curing agent was then added to the mixture according to the mass ratio 10:1 of PDMS base to the curing agent. For the CB/MXene/PDMS, the fabrication procedures were similar to those of CB/PDMS, but the monolayer MXene with 1, 2, 3, and 4 wt % was added together with the CB into the PDMS diluent.

4.2. Fabrication of the SMFS. After stirring with the curing agent and degassing, the CB/PDMS or CB/MXene/PDMS was cast into polytetrafluoroethylene (PTFE) molds with the cone structure in the middle. Then, the CB/PDMS or CB/MXene/PDMS together with the mold was cured at 80 °C for 3 h. After the composite was cured, four round copper electrodes connected with copper wires were attached to the upper surface of the composite cone with the aid of silver paste. Subsequently, pure liquid PDMS was poured on the electrodes as the encapsulation and the hollow cylinders were filled in the mold as the supporting structure. After degassing, the uncured PDMS was heated at 80 °C for another 3 h to fully solidify the PDMS. The whole device integrated with the supporting structure, cone, and the electrodes was demolded from the PTFE mold together. Besides the cone structure, two different sensing structures, including the cylinder and cuboid, were also fabricated. These sensors were all made of PDMS, and the fabrication process was the same as that of the CB/PDMS or CB/MXene/PDMS samples. Finally, the as-obtained samples were assembled by attaching the supporting structure to Al-coated PET substrates.

4.3. Characterization and Measurement. The morphologies of the samples were obtained using a field-emission scanning electron microscope (NOVA 450). An ESM301/Mark-10 system was used for the cyclic press-release test, and a Mark-10 force gauge was used to detect the applied force and corresponding displacement under compression. The pressing rate was 100 mm/min for the measurement and changed from 10 to 150 mm/min for the speed dependence test. To achieve normal, tilt, and shear force sensing via vertical

https://doi.org/10.1021/acsami.2c03812
ACS Appl. Mater. Interfaces 2022, 14, 20122−20131

movement of the force gauge, acrylic covers with different planes at different angles were attached to the force gauge and test platform. The V_{OC} of the SMFS was measured using a Keithley 6517 electrometer and was recorded through an oscilloscope (LeCroy HDO6104).

■ ASSOCIATED CONTENT

Supporting Information

The Supporting Information is available free of charge at https://pubs.acs.org/doi/10.1021/acsami.2c03812.

Electrical potential distribution simulation (MP4)

Four-channel data acquisition for force detection (MP4)

Smart direction indicator system (MP4)

Surface SEM images of CB/PDMS and CB/MXene/PDMS composites with various filler contents; cross-section view of the SEM image of C_2M_3; experimental setup used to characterize the SMFS; V_{OC} responses of different sensing structures under applied normal forces of 2, 5, and 10 N; comparison of V_{OC} responses of the cone sensing structure with different CB filling contents under applied normal force ranging from 1 to 15 N; force−displacement relationship curves of C_2M_3 under applied normal, tilt, and shear forces; representative response curves of C_2M_3 under tilt and shear forces; relationship curve of V_{OC} responses of the SMFS with different CB/Mxene contents under pressure induced by normal force, tilt force, and shear force; comparison of V_{OC} responses of the cone sensing structure made of PDMS, C_2, and C_2M_3 under applied normal pressure ranging from 5.1 to 76.5 kPa; one loading and unloading cycle of applied 1 N normal force; V_{OC} responses and applied 8 N normal force curves under periodic loading and unloading cycles; demonstration of distinguishing the force direction through four-channel signals; ability of distinguishing the direction of tilt force with demonstration of four-channel signals; and electric circuit diagram of the indicator system with detailed connections (PDF)

■ AUTHOR INFORMATION

Corresponding Authors

Yubo Fan − *Key Laboratory for Biomechanics and Mechanobiology of Ministry of Education, Beijing Advanced Innovation Center for Biomedical Engineering, School of Biological Science and Medical Engineering, Beihang University, Beijing 100191, China; School of Engineering Medicine, Beihang University, Beijing 100191, China;* Email: yubofan@buaa.edu.cn

Bojing Shi − *Key Laboratory for Biomechanics and Mechanobiology of Ministry of Education, Beijing Advanced Innovation Center for Biomedical Engineering, School of Biological Science and Medical Engineering, Beihang University, Beijing 100191, China;* orcid.org/0000-0003-0802-8326; Email: bjshi@buaa.edu.cn

Zhou Li − *Beijing Key Laboratory of Micro-nano Energy and Sensor, Beijing Institute of Nanoenergy and Nanosystems, Chinese Academy of Sciences, Beijing 101400, China; School of Nanoscience and Technology, University of Chinese Academy of Sciences, Beijing 100049, China; Center on Nanoenergy Research, School of Physical Science and Technology, Guangxi University, Nanning 530004, China; Institute for Stem Cell and Regeneration, Chinese Academy of Sciences, Beijing 100101, China;* orcid.org/0000-0002-9952-7296; Email: zli@binn.cas.cn

Authors

Weiyi Zhang − *Beijing Key Laboratory of Micro-nano Energy and Sensor, Beijing Institute of Nanoenergy and Nanosystems, Chinese Academy of Sciences, Beijing 101400, China; School of Microelectronics, Tianjin University, Tianjin 300072, China*

Yuan Xi − *Beijing Key Laboratory of Micro-nano Energy and Sensor, Beijing Institute of Nanoenergy and Nanosystems, Chinese Academy of Sciences, Beijing 101400, China; Key Laboratory for Biomechanics and Mechanobiology of Ministry of Education, Beijing Advanced Innovation Center for Biomedical Engineering, School of Biological Science and Medical Engineering, Beihang University, Beijing 100191, China*

Engui Wang − *Beijing Key Laboratory of Micro-nano Energy and Sensor, Beijing Institute of Nanoenergy and Nanosystems, Chinese Academy of Sciences, Beijing 101400, China; Center on Nanoenergy Research, School of Physical Science and Technology, Guangxi University, Nanning 530004, China*

Xuecheng Qu − *Beijing Key Laboratory of Micro-nano Energy and Sensor, Beijing Institute of Nanoenergy and Nanosystems, Chinese Academy of Sciences, Beijing 101400, China; School of Nanoscience and Technology, University of Chinese Academy of Sciences, Beijing 100049, China*

Yuan Yang − *Beijing Key Laboratory of Micro-nano Energy and Sensor, Beijing Institute of Nanoenergy and Nanosystems, Chinese Academy of Sciences, Beijing 101400, China; School of Nanoscience and Technology, University of Chinese Academy of Sciences, Beijing 100049, China*

Complete contact information is available at: https://pubs.acs.org/10.1021/acsami.2c03812

Author Contributions

W.Z. and Y.X. contributed equally. Z.L., B.S., and Y.F. supervised the project. W.Z., Y.X., and B.S. conceived the idea and designed the experiments. W.Z. and Y.Y. fabricated the devices. W.Z. conducted the device performance characterization. W.Z., Y.X., E.W., and X.Q. accomplished the material characterization. W.Z., Y.X., B.S., Y.F., and Z.L. wrote the article, and all authors reviewed and commented on the article. All authors have given approval to the final version of the article.

Notes

The authors declare no competing financial interest.

■ ACKNOWLEDGMENTS

The authors are grateful for the support received from the National Natural Science Foundation of China (T2125003, 61875015, 32101117, U20A20390, and 11827803), the Strategic Priority Research Program of the Chinese Academy of Sciences (XDA16021101), the Beijing Natural Science Foundation (JQ20038, L212010), and the Fundamental Research Funds for the Central Universities.

■ REFERENCES

(1) Billard, A.; Kragic, D. Trends and Challenges in Robot Manipulation. *Science* **2019**, *364*, No. eaat8414.

(2) Yang, J. C.; Mun, J.; Kwon, S. Y.; Park, S.; Bao, Z.; Park, S. Electronic Skin: Recent Progress and Future Prospects for Skin-

Attachable Devices for Health Monitoring, Robotics, and Prosthetics. *Adv. Mater.* **2019**, *31*, 1904765.
(3) Chen, J.; Zhu, Y.; Chang, X.; Pan, D.; Song, G.; Guo, Z.; Naik, N. Recent Progress in Essential Functions of Soft Electronic Skin. *Adv. Funct. Mater.* **2021**, *31*, 2104686.
(4) Yan, S.-H.; Liu, Y.-C.; Li, W.; Zhang, K. Gait Phase Detection by Using a Portable System and Artificial Neural Network. *Med. Nov. Technol. Dev.* **2021**, *12*, 100092.
(5) He, F.; You, X.; Wang, W.; Bai, T.; Xue, G.; Ye, M. Recent Progress in Flexible Microstructural Pressure Sensors toward Human-Machine Interaction and Healthcare Applications. *Small Methods* **2021**, *5*, 2001041.
(6) Wang, L.; Zhang, M.; Yang, B.; Tan, J.; Ding, X.; Li, W. Recent Advances in Multidimensional (1D, 2D, and 3D) Composite Sensors Derived from MXene: Synthesis, Structure, Application, and Perspective. *Small Methods* **2021**, *5*, 2100409.
(7) Boutry, C. M.; Beker, L.; Kaizawa, Y.; Vassos, C.; Tran, H.; Hinckley, A. C.; Pfattner, R.; Niu, S.; Li, J.; Claverie, J.; Wang, Z.; Chang, J.; Fox, P. M.; Bao, Z. Biodegradable and Flexible Arterial-Pulse Sensor for the Wireless Monitoring of Blood Flow. *Nat. Biomed. Eng.* **2019**, *3*, 47−57.
(8) Ouyang, H.; Tian, J.; Sun, G.; Zou, Y.; Liu, Z.; Li, H.; Zhao, L.; Shi, B.; Fan, Y.; Fan, Y.; Wang, Z. L.; Li, Z. Self-Powered Pulse Sensor for Antidiastole of Cardiovascular Disease. *Adv. Mater.* **2017**, *29*, 1703456.
(9) Gao, Y.; Yu, L.; Yeo, J. C.; Lim, C. T. Flexible Hybrid Sensors for Health Monitoring: Materials and Mechanisms to Render Wearability. *Adv. Mater.* **2020**, *32*, 1902133.
(10) Boutry, C. M.; Negre, M.; Jorda, M.; Vardoulis, O.; Chortos, A.; Khatib, O.; Bao, Z. A Hierarchically Patterned, Bioinspired E-Skin Able to Detect the Direction of Applied Pressure for Robotics. *Sci. Rob.* **2018**, *3*, No. eaau6914.
(11) Won, Y.; Lee, J. J.; Shin, J.; Lee, M.; Kim, S.; Gandla, S. Biocompatible, Transparent, and High-Areal-Coverage Kirigami PEDOT:PSS Electrodes for Electrooculography-Derived Human−Machine Interactions. *ACS Sens.* **2021**, *6*, 967−975.
(12) Yin, R.; Wang, D.; Zhao, S.; Lou, Z.; Shen, G. Wearable Sensors-Enabled Human−Machine Interaction Systems: From Design to Application. *Adv. Funct. Mater.* **2021**, *31*, 2008936.
(13) Wu, Y.; Liu, Y.; Zhou, Y.; Man, Q.; Hu, C.; Asghar, W.; Li, F.; Yu, Z.; Shang, J.; Liu, G.; Liao, M.; Li, R.-W. A Skin-Inspired Tactile Sensor for Smart Prosthetics. *Sci. Rob.* **2018**, *3*, No. eaat0429.
(14) Yang, J. C.; Kim, J.-O.; Oh, J.; Kwon, S. Y.; Sim, J. Y.; Kim, D. W.; Choi, H. B.; Park, S. Microstructured Porous Pyramid-Based Ultrahigh Sensitive Pressure Sensor Insensitive to Strain and Temperature. *ACS Appl. Mater. Interfaces* **2019**, *11*, 19472−19480.
(15) Choi, W.; Lee, J.; Yoo, Y. K.; Kang, S.; Kim, J.; Lee, J. H. Enhanced Sensitivity of Piezoelectric Pressure Sensor with Microstructured Polydimethylsiloxane Layer. *Appl. Phys. Lett.* **2014**, *104*, 123701.
(16) Bai, N.; Wang, L.; Wang, Q.; Deng, J.; Wang, Y.; Lu, P.; Huang, J.; Li, G.; Zhang, Y.; Yang, J.; Xie, K.; Zhao, X.; Guo, C. F. Graded Intrafillable Architecture-Based Iontronic Pressure Sensor with Ultra-Broad-Range High Sensitivity. *Nat. Commun.* **2020**, *11*, 209.
(17) Ruth, S. R. A.; Feig, V. R.; Tran, H.; Bao, Z. Microengineering Pressure Sensor Active Layers for Improved Performance. *Adv. Funct. Mater.* **2020**, *30*, 2003491.
(18) Shao, S.; Wu, J.; Zhou, Q. Developments and Challenges in Human Performance Enhancement Technology. *Med. Nov. Technol. Dev.* **2021**, *12*, 100095.
(19) Wang, Z.; Bu, T.; Li, Y.; Wei, D.; Tao, B.; Yin, Z.; Zhang, C.; Wu, H. Multidimensional Force Sensors Based on Triboelectric Nanogenerators for Electronic Skin. *ACS Appl. Mater. Interfaces* **2021**, *13*, 56320−56328.
(20) Chen, T.; Shi, Q.; Yang, Z.; Liu, J.; Liu, H.; Sun, L.; Lee, C. A Self-Powered Six-Axis Tactile Sensor by Using Triboelectric Mechanism. *Nanomaterials* **2018**, *8*, 503.
(21) Lin, L.; Xie, Y.; Wang, S.; Wu, W.; Niu, S.; Wen, X.; Wang, Z. L. Triboelectric Active Sensor Array for Self-Powered Static and Dynamic Pressure Detection and Tactile Imaging. *ACS Nano* **2013**, *7*, 8266−8274.
(22) Zou, Y.; Liao, J.; Ouyang, H.; Jiang, D.; Zhao, C.; Li, Z.; Qu, X.; Liu, Z.; Fan, Y.; Shi, B.; Zheng, L.; Li, Z. A Flexible Self-Arched Biosensor Based on Combination of Piezoelectric and Triboelectric Effects. *Appl. Mater. Today* **2020**, *20*, 100699.
(23) Li, Y.; Cao, Z.; Li, T.; Sun, F.; Bai, Y.; Lu, Q.; Wang, S.; Yang, X.; Hao, M.; Lan, N.; Zhang, T. Highly Selective Biomimetic Flexible Tactile Sensor for Neuroprosthetics. *Research* **2020**, *2020*, 8910692.
(24) Guo, H.; Tan, Y. J.; Chen, G.; Wang, Z.; Susanto, G. J.; See, H. H.; Yang, Z.; Lim, Z. W.; Yang, L.; Tee, B. C. K. Artificially Innervated Self-Healing Foams as Synthetic Piezo-Impedance Sensor Skins. *Nat. Commun.* **2020**, *11*, 5747.
(25) Ren, Z.; Nie, J.; Shao, J.; Lai, Q.; Wang, L.; Chen, J.; Chen, X.; Wang, Z. L. Fully Elastic and Metal-Free Tactile Sensors for Detecting both Normal and Tangential Forces Based on Triboelectric Nanogenerators. *Adv. Funct. Mater.* **2018**, *28*, 1802989.
(26) Dai, J.; Li, L.; Shi, B.; Li, Z. Recent Progress of Self-Powered Respiration Monitoring Systems. *Biosens. Bioelectron.* **2021**, *194*, 113609.
(27) Xia, X.; Chen, J.; Liu, G.; Javed, M. S.; Wang, X.; Hu, C. Aligning Graphene Sheets in PDMS for Improving Output Performance of Triboelectric Nanogenerator. *Carbon* **2017**, *111*, 569−576.
(28) Qiu, Y.; Tian, Y.; Sun, S.; Hu, J.; Wang, Y.; Zhang, Z.; Liu, A.; Cheng, H.; Gao, W.; Zhang, W.; Chai, H.; Wu, H. Bioinspired, Multifunctional Dual-Mode Pressure Sensors as Electronic Skin for Decoding Complex Loading Processes and Human Motions. *Nano Energy* **2020**, *78*, 105337.
(29) Qin, J.; Yin, L. J.; Hao, Y. N.; Zhong, S. L.; Zhang, D. L.; Bi, K.; Zhang, Y. X.; Zhao, Y.; Dang, Z. M. Flexible and Stretchable Capacitive Sensors with Different Microstructures. *Adv. Mater.* **2021**, *33*, 2008267.
(30) Li, X.; Li, X.; Liu, T.; Lu, Y.; Shang, C.; Ding, X.; Zhang, J.; Feng, Y.; Xu, F.-J. Wearable, Washable, and Highly Sensitive Piezoresistive Pressure Sensor Based on a 3D Sponge Network for Real-Time Monitoring Human Body Activities. *ACS Appl. Mater. Interfaces* **2021**, *13*, 46848−46857.
(31) Cai, Y.-W.; Zhang, X.-N.; Wang, G.-G.; Li, G.-Z.; Zhao, D.-Q.; Sun, N.; Li, F.; Zhang, H.-Y.; Han, J.-C.; Yang, Y. A Flexible Ultra-Sensitive Triboelectric Tactile Sensor of Wrinkled PDMS/MXene Composite Films for E-Skin. *Nano Energy* **2021**, *81*, 105663.
(32) Pierre Claver, U.; Zhao, G. Recent Progress in Flexible Pressure Sensors Based Electronic Skin. *Adv. Eng. Mater.* **2021**, *23*, 2001187.
(33) Hatta, F. F.; Mohammad Haniff, M. A. S.; Mohamed, M. A. A Review on Applications of Graphene in Triboelectric Nanogenerators. *Int. J. Energy Res.* **2021**, *46*, 544.
(34) Zhang, W.; Liu, Q.; Chao, S.; Liu, R.; Cui, X.; Sun, Y.; Ouyang, H.; Li, Z. Ultrathin Stretchable Triboelectric Nanogenerators Improved by Postcharging Electrode Material. *ACS Appl. Mater. Interfaces* **2021**, *13*, 42966−42976.
(35) Luo, X.; Zhu, L.; Wang, Y. C.; Li, J.; Nie, J.; Wang, Z. L. A Flexible Multifunctional Triboelectric Nanogenerator Based on MXene/PVA Hydrogel. *Adv. Funct. Mater.* **2021**, *31*, 2104928.
(36) Salauddin, M.; Rana, S. M. S.; Sharifuzzaman, M.; Rahman, M. T.; Park, C.; Cho, H.; Maharjan, P.; Bhatta, T.; Park, J. Y. A Novel MXene/Ecoflex Nanocomposite-Coated Fabric as a Highly Negative and Stable Friction Layer for High-Output Triboelectric Nanogenerators. *Adv. Energy Mater.* **2021**, *11*, 2002832.
(37) Chen, H.; Song, Y.; Guo, H.; Miao, L.; Chen, X.; Su, Z.; Zhang, H. Hybrid Porous Micro Structured Finger Skin Inspired Self-Powered Electronic Skin System for Pressure Sensing and Sliding Detection. *Nano Energy* **2018**, *51*, 496−503.
(38) Wang, Z. L.; Wang, A. C. On the Origin of Contact-Electrification. *Mater. Today* **2019**, *30*, 34−51.

https://doi.org/10.1021/acsami.2c03812
ACS Appl. Mater. Interfaces 2022, 14, 20122−20131